

Method of measuring charge distribution of nanosized aerosols

S.H. Kim, K.S. Woo, B.Y.H. Liu, M.R. Zachariah*

Departments of Mechanical Engineering and Chemistry, University of Minnesota, USA

Received 18 February 2004; accepted 13 August 2004

Available online 11 September 2004

Abstract

In this paper, we present the development of a method to accurately measure the positive and negative charge distribution of nanosized aerosols using a tandem differential mobility analyzer (TDMA) system. From the series of TDMA measurements, the charge fraction of nanosized aerosol particles was obtained as a function of equivalent mobility particle diameter ranging from 50 to 200 nm. The capability of this new approach was implemented by sampling from a laminar diffusion flame which provides a source of highly charged particles due to naturally occurring flame ionization process. The results from the TDMA measurement provide the charge distribution of nanosized aerosols which we found to be in reasonable agreement with Boltzmann equilibrium charge distribution theory and a theory based upon charge population balance equation (PBE) combined with Fuchs theory (N.A. Fuchs, *Geofis. Pura Appl.* 56 (1963) 185). The theoretically estimated charge distribution of aerosol particles based on the PBE provides insight into the charging processes of nanosized aerosols surrounded by bipolar ions and electrons, and agree well with the TDMA results.

© 2004 Elsevier Inc. All rights reserved.

Keywords: Nanosized aerosols; Positive ion; Negative ion; Electron; Tandem differential mobility analyzer; Boltzmann theory; Charge population balance equation; Diffusion flame

1. Introduction

The charge of an aerosol has an important effect on its sampling, transport, deposition, and collection by filtration. To accurately assess the role of charge and electrical effects in practical devices it is important to know the aerosol charge distribution as a function of particle size. Researchers have developed several approaches and charge analyzers to measure the particle charge distribution. Integral mobility techniques have been developed to provide the magnitude of charge of solid and liquid particles [1–4]. However, a disadvantage of the integral mobility technique is its inability to provide the polarity of the particle charge. Another approach involves the use of a differential mobility analyzer (DMA) coupled to an optical aerosol spectrometer to measure the charge distribution of particles [5]. However, in that study the size detection limit of the optical aerosol spectrometer

limited the range of measurement to relatively large particles (0.5–2 μm).

In practical combustion systems, the emitted aerosol particles are typically in the size regime of 10–200 nm [6,7] and even though aerosol charging mechanisms in combustion process are reasonably well understood, the techniques for characterizing the charge distribution of nanosized combustion aerosol are not satisfactorily developed. Moon [6] applied the tandem differential mobility analyzer (TDMA) technique to monitor the evolution of charge distribution of combustion particles generated from various diesel engine loading conditions. However, because of a rather low resolution of electrical aerosol analyzer used in that study, doubly and more highly charged particles were not accurately detected. Recently, Ahn et al. [8] also used a TDMA system to measure the charge distribution of SiO_2 particles produced in $\text{H}_2/\text{O}_2/\text{TEOS}$ diffusion flame. They determined the ratio (N_1/N_2) of the singly to doubly charged silica particles as a function of particle size. It was observed that the ratio (N_1/N_2) is highly deviated from that of Fuchs equilibrium charge at a small particle size regime (10–200 nm) in vari-

* Corresponding author.

E-mail address: mrz@umd.edu (M.R. Zachariah).

ous flame regions. However, in their study, the fractions of uncharged and charged particles were not considered. Furthermore, the detailed procedures for obtaining the particle charge distribution, which require special attention, were not presented.

In this paper, we describe a modified TDMA method to accurately measure the charge and size distribution of nano-aerosols. The basic approach of the TDMA method which will be outlined in this paper has been applied to a variety of aerosol related problems including measurement of evaporation, condensation, hydrophobicity, and chemical reactivity [9–11]. The TDMA data processing procedure is also presented to determine both the positive and negative particle charge distribution as a function of mobility size of particle extracted from an Collison atomizer and a diffusion flame, respectively. The TDMA generated charge distributions of nanoaerosols are compared with theoretical calculations based on Boltzmann charging theory and a charge population balance equation.

2. Experimental

To generate highly charged nanosized soot aerosols, we built a diffusion flame burner system, which consists of a

1.25 cm central tube for fuel and a 10 cm outer tube for air supply [11,12]. Dry, filtered air penetrates through the outer tube, which contains uniformly perforated air distribution plate, glass beads, fine meshes, and a ceramic honeycomb in order to condition the flow. A glass shield was used around the burner to minimize any external disturbances. The flame burner was fueled by ethylene with a mixing ratio of fuel:air = 1:500. For the current experiment, 0.1 L min^{-1} of ethylene and 50 L min^{-1} of air were provided to support a 5 cm long diffusion flame. Fig. 1 depicts the schematic of the diffusion flame burner system. A stainless steel sampling probe with an outer diameter of 1.25 cm and with a sampling orifice of 0.1 cm in diameter was horizontally positioned just at the visible flame tip [11,13]. Soot particles were sampled through the orifice via the venturi effect, by passing a diluting carrier gas (10 L min^{-1}) through the sampling tube. The soot particles were rapidly diluted with two transvacuum pumps with a designed dilution ratio of 1/100.

Fig. 1 also shows a schematic of the TDMA system. The TDMA consists of two differential mobility analyzers (DMAs) and a condensation nucleus counter (CNC). A DMA operates by balancing the electrical force on a charged particle in an applied field, with the drag force on the particle as it moves through the fluid. The in-house built

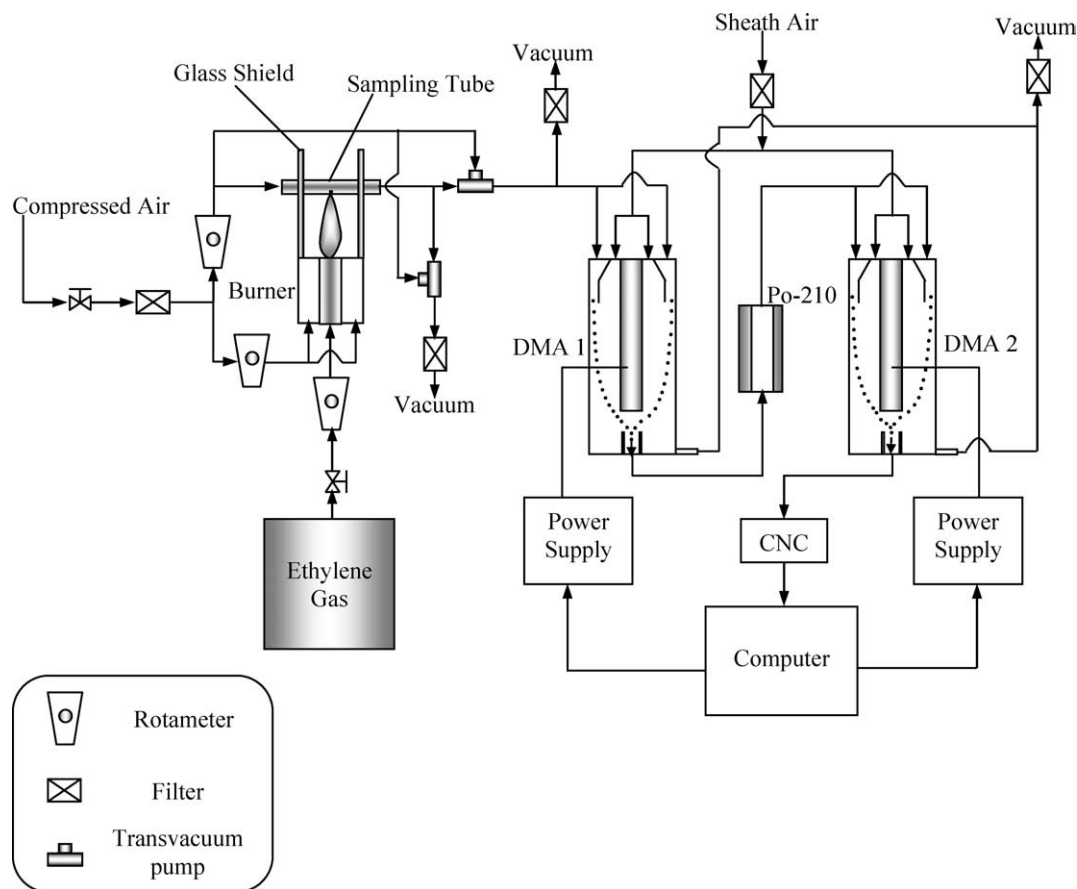


Fig. 1. Schematic diagram of TDMA experiment for measuring soot particle charge and size distribution (DMA, differential mobility analyzer; CNC, condensation nuclei counter).

DMA consists of a cylindrical central electrode and a coaxially aligned cylindrical stainless steel housing. Filtered, dry air is supplied in the annular region around the central electrode, and an annular flow of sampled aerosol is introduced from the top of the DMA column. Here aerosol is normally passed through a radioactive ionizing source, which have the aerosol become charged to a known charge level. Aerosol particles enter the DMA in a thin annular ring adjacent to the outer cylinder, and the charged particles are attracted or repelled by the potential on the center rod. Near the end of the center rod is a slit through which particles of the desired electric mobility pass, while particles of higher electric mobility (particles that are smaller and/or more highly charged) hit the center rod upstream of the sample slit and particles of lower electric mobility (larger and/or uncharged) pass out of the DMA through the excess output flow [14–16].

The particle electrical mobility is defined as [17]

$$Z_p = \frac{peC_c(d_p)}{3\pi\mu d_p}, \quad (1)$$

where p is the number of elementary units of charge, $C_c(d_p)$ is the Cunningham slip correction factor ($= 1 + 2.514\lambda/d_p + 0.8\lambda/d_p \exp(-0.55d_p/\lambda)$), λ is the mean free path of air, and μ is the viscosity of air.

Unlike a normal DMA system, DMA-1 is simply used as an electrical field classifying system, which is operated at a chosen fixed voltage to extract particles of equivalent electrical mobility without employing a radioactive ionizing source prior to DMA-1 (see Fig. 1). The DMA-2 then scans the size distribution of particles selected from the DMA-1. The CNC counts the particles by growing them via heterogeneous condensation of supersaturated butanol to a size amenable for optical detection.

We evaluated the particle TDMA transfer function using NaCl particles generated with a Collision atomizer and followed the procedure outlined by Stolzenburg and McMurry [18]. The final calibration of the TDMA yields three parameters used to quantify the quality of the transfer function; f_N is the fraction of particles leaving DMA-1 that are detected in a given DMA-2 peak, f_V the mobility growth factor for a given DMA-2 peak (or the ratio of centroid mobilities of DMA-1 and DMA-2), and f_β the correction factor for width of particle size distribution detected by DMA-2. Ideally these three parameters should be unity. The values for our system were $f_N = 0.95 \pm 0.02$, $f_V = 1.02 \pm 0.002$, and $f_\beta = 1.06 \pm 0.02$. Also the final diameter ratio of a particle selected by both DMA-1 and DMA-2 was 1.012 ± 0.002 , or a measurement error of less than 1%.

Quantitative information on flame temperature was obtained in both the radial and axial direction using a 0.3 mm diameter fine wire thermocouple shown in Fig. 2. The Pt/Rh fine wire thermocouple was manually inserted in various locations of the flame zone and temperatures were recorded as an average over five measurements to minimize the errors associated with carbon deposition to the thermocouple wire. The temperature at the flame tip in the presence of the

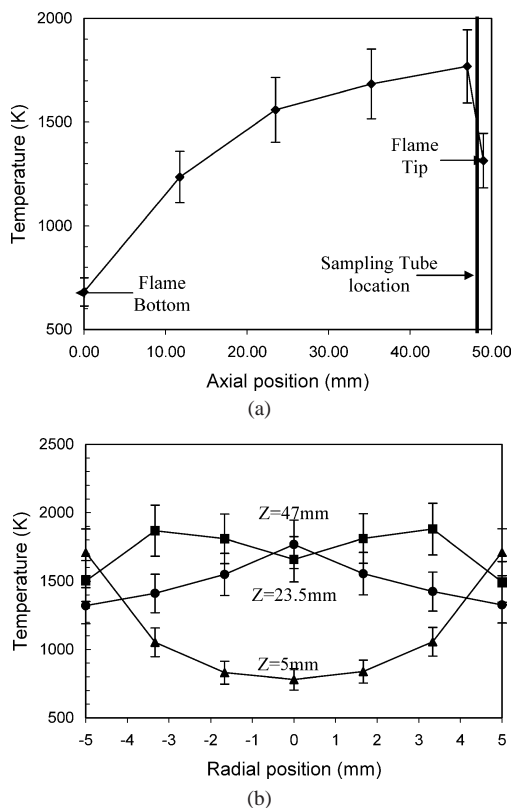


Fig. 2. Flame temperature distribution measured with fine wire thermocouples. (a) Axial direction along centerline. (b) Radial direction at flame heights of $z = 5, 23.5,$ and 47 mm from burner lip.

sampling tube was measured by inserting the thermocouple within the sampling orifice. As has been observed by Santoro [7] and characteristic of co-annular diffusion flames, peak temperatures at short distances above the nozzle occur in an annular region. With increasing height in the flame the annular region decreases in radius till the flame tip and it is here that we place our sampling tube.

In order to evaluate the particle charging rate in the flame and relate that to the measured particle charge distribution, we measured concentrations of positive ions and electrons with a Langmuir probe, following procedures described in the literature [19,20].

Two fine tungsten wires with radius of 0.015 cm and a separation distance of 1 mm were used to minimize the disturbance to the flame. The data are processed under the assumption that the voltage difference (V_d) between the wires has no effect on the ion current in the flame and that all charge carriers arriving at the plasma sheath are collected by the probe with unit efficiency.

Probe-1 was connected to the reference voltage, while probe-2 was connected to a pico-ammeter to read the induced current. By sweeping a range of voltages in probe-1, we recorded the corresponding currents from probe-2. When the potential of probe-1 is negative, electrons are repelled and the current is dominated by positive ions. At sufficiently large negative voltages, probe-1 operates under a saturation current of positive ions, which is balanced by an electron

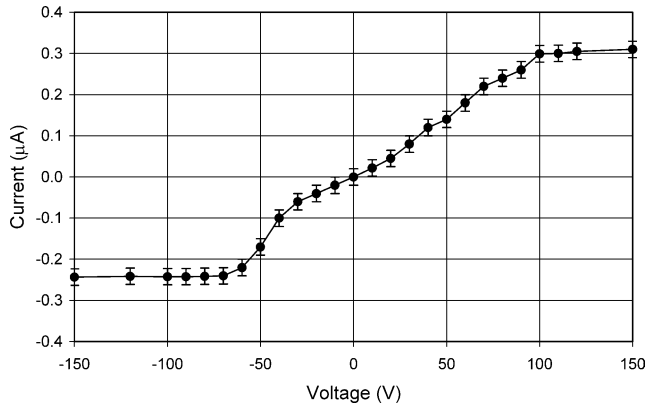


Fig. 3. Langmuir double-probe measurement of voltage–current relationship in a diffusion flame (flame tip).

current to probe-2. However, when probe-1 is biased sufficiently positive, the ion current is reduced, and the electron current dominates so that a saturation current of electrons in probe-1 is in steady state with the positive ion current to probe-2.

Fig. 3 shows an example of a Langmuir probe voltage–current characteristic curve obtained at the flame tip, where the soot particles were sampled. By ramping the voltage we determine the saturation current for positive ions and electrons. The saturation currents obtained were 0.30 and $-0.22 \mu\text{A}$ from an applied voltage of 100 and -70 V , and corresponded to concentrations of positive ions and electrons of 3.5×10^{11} and $1.5 \times 10^7 \text{ cm}^{-3}$, respectively, as calculated by the equation [20,21]

$$j = n_i e \left(\frac{kT}{2\pi M} \right)^{1/2} \left\{ 1 + \frac{1.5Lr_p}{4\lambda B} \ln \left(\frac{X+B}{X-B} \right) \right\}^{-1}, \quad (2)$$

where j is the ion current density, n_i the concentration of ions, L the probe length immersed in the flame, r_p the probe radius, T the ion temperature, M the molecular weight of the ion, λ is the mean free path of air, $X = L + 2\lambda_i$, λ_i is the mean free path of ions, and $B = \sqrt{X^2 - 4(r_p + \lambda_i)^2}$.

It was assumed that H_3O^+ is the primary representative positive ion carrier since it is considered to be one of the major ions generated by chemi-ionization in flames [22,23]. The temperatures of ions and electrons are assumed to be thermalized to the neutral gas temperature.

Mass spectrometric measurements [24] have found that the mass of negative charge carriers is typically lighter than positive ones, and that the carriers are mostly associated with carbonless ions like OH^- near the flame tip, while hydrocarbon ions are found to be the main negative charge carriers inside the flame. Since the flame is a quasineutral thermal plasma, the number concentration of positive ions must equal the number concentration of negative ions plus electrons ($n^+ = n^- + n_e$) at any location in the flame [25,26]. On this basis we can readily calculate the number concentration of negative ions, which is of similar concentration with positive ions, due to the small concentration of elec-

trons compared with that of positive ions as measured by the Langmuir double probe.

3. Experimental results: comparison with theory

3.1. Principle of TDMA technique for charge measurement

Fig. 4 illustrates the TDMA system as used to detect multiply charged flame generated particles. To determine the fraction of multiply charged particles (f_p or N_p/N_T ; p is the number of elementary unit of charge) as a function of equivalent mobility particle size, we need to measure a particle number concentration (N_T) for each particle size. We determined the total particle concentration as a function of size by converting the TDMA system to a differential mobility particle sizer (DMPS) [27] configuration by employing only DMA-1 and the CNC (see path (A) in Fig. 4). In this configuration a Po-210 ionizing radiation source, typically termed a “neutralizer,” is employed prior to DMA-1 to provide a bath of bipolar ions and therefore a known Boltzmann charge distribution to the aerosol [15]. The resulting diluted flame soot size distribution is shown in Fig. 5a. Then to measure the particle concentration carrying p charges at a particular particle size ($N_p(d)$), the TDMA system was employed (see path (B) in Fig. 4).

To detect positively charged particles, for example, the charged soot particles of both polarities are introduced into DMA-1. DMA-1, which is operated with a negatively charged electrode, selects for positively charged particles of equivalent electrical mobility. While these particles have equivalent mobility, they are not necessarily of the same size due to multiple charging effects. To separate the particles further, these same electrical mobility particles selected in DMA-1 are passed through the ionizing radioactive source (Po-210). The source bombards the particles with bipolar ions and is known to produce an aerosol with a Boltzmann charge distribution. The distribution is computed by the equation [17]

$$f_{p,B} = \frac{2e}{(\pi d_p kT)^{1/2}} \exp\left(-\frac{p^2 e^2}{d_p kT}\right), \quad (3)$$

where e is the elementary electrical charge, d_p the particle diameter, k Boltzmann’s constant, T the temperature, and p the number of elementary unit of charge.

Equation (3) describes the fraction of particles with a charge p , temperature T , and particle diameter d_p . From the DMA-2 measurement of the Boltzmannized mobility diameter distribution, we observed multiple peaks in the particle size distribution. These correspond to a group of particles which when sampled from DMA-1 had equivalent electrical mobility. These particles with equivalent mobility coming from DMA-1 are a mixture of large particles with many charges or small particles with unity charge.

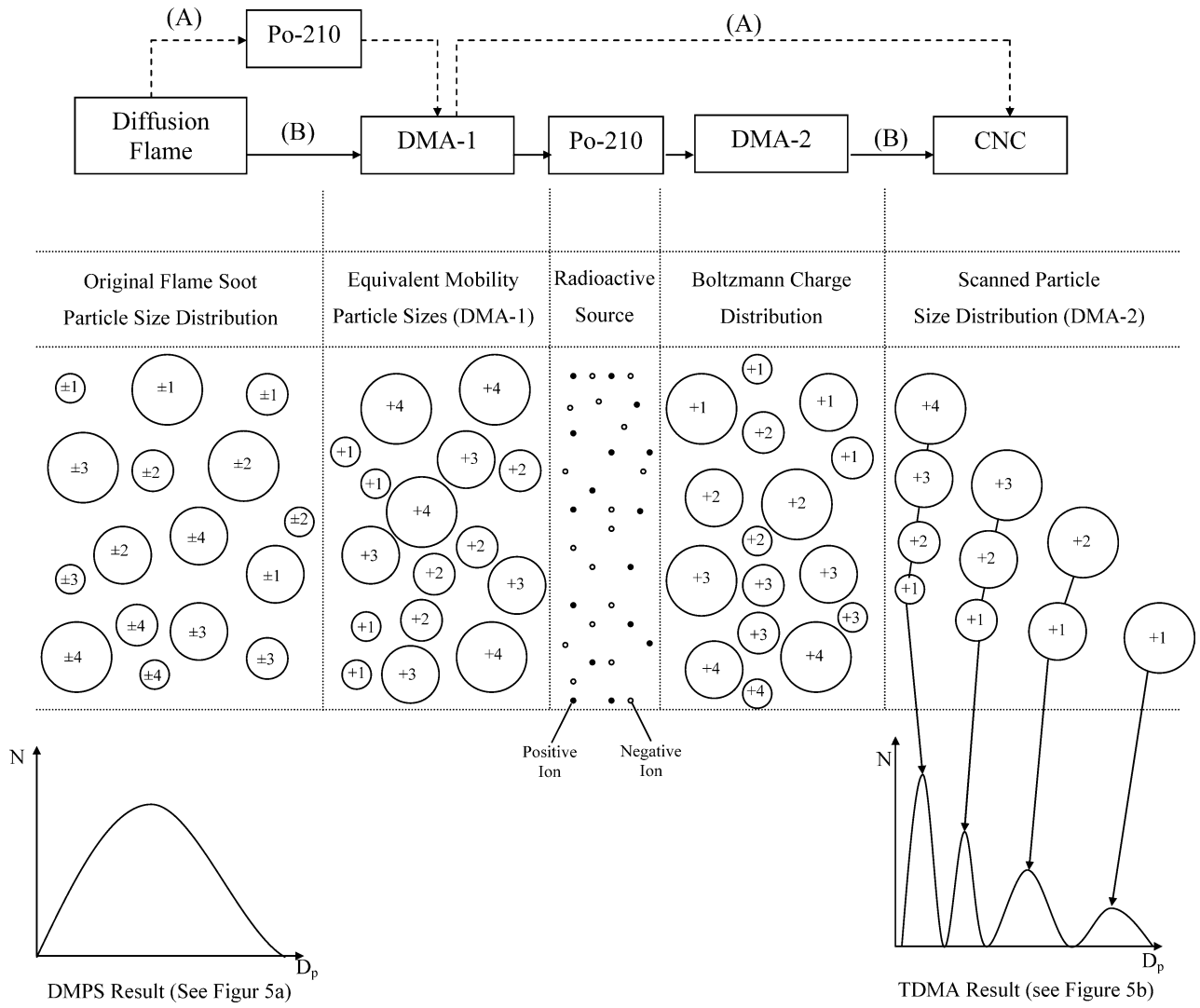


Fig. 4. Schematic diagram of DMPS and TDMA system used to measure the charge and size distribution of flame soot particles (path (A), DMPS system; path (B), TDMA system).

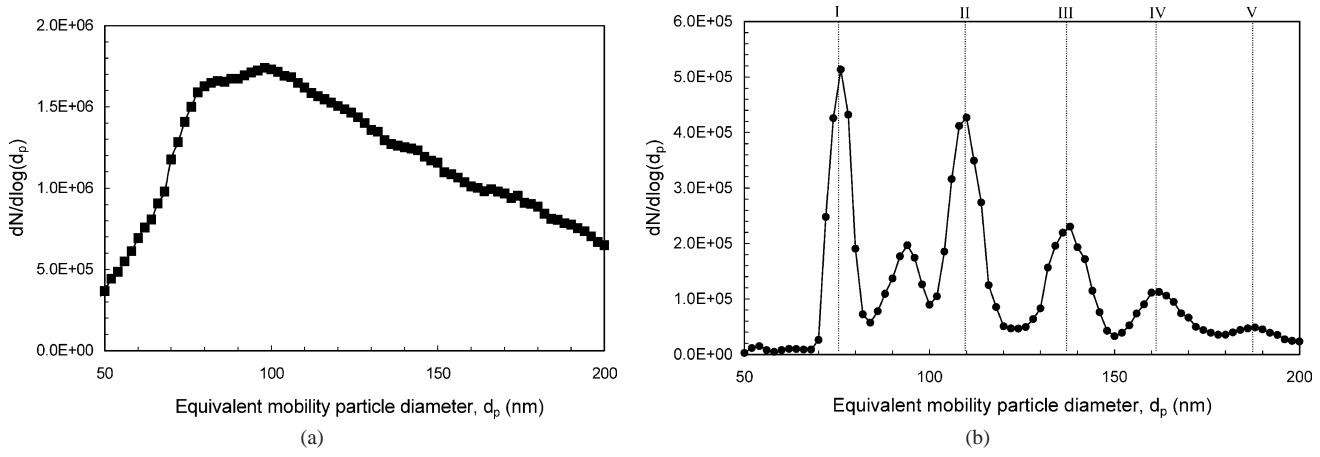


Fig. 5. (a) DMPS measurement of nanosized flame soot particles and (b) an example TDMA measurement of nanosized flame soot particles; DMA-1 set to $Z_p = 4.5 \times 10^{-11}$ C cm/dyn s (corresponds to equivalent mobility size of 75 nm with single charge).

Table 1

Comparison of the calculated multiple peaks of particle size distribution with experimental data detected by DMA-2 at an electrical mobility of 4.5×10^{-11} C cm/dyn s corresponding to mobility size of 75 nm in DMA-1

DMA-1			Boltzmann charge distribution				Estimated DMA-2 peak		Measured DMA-2 peak
$Z_p \times 10^{-11}$ (C cm/dyn s)	d_p (nm)	Charge (unit)	$Z_p \times 10^{-11}$ (C cm/dyn s)	d_p (nm)	p (unit)	$f_{p,B}$	d_p (nm)	d_p (nm)	
4.5	76	+1	4.5	75	+1	0.231	75	76	
			9.0	75	+2	0.024	51	54	
			13.6	75	+3	0.000	41	–	
			18.1	75	+4	0.000	35	–	
			22.6	75	+5	0.000	31	–	
	113	+2	2.2	113	+1	0.242	113	110	
			4.4	113	+2	0.053	75	76	
			6.6	113	+3	0.004	61	64	
			8.9	113	+4	0.000	52	54	
			11.1	113	+5	0.000	46	–	
	145	+3	1.5	145	+1	0.239	145	138	
			2.9	145	+2	0.073	97	94	
			4.4	145	+3	0.010	75	76	
			5.9	145	+4	0.001	65	64	
			7.3	145	+5	0.000	58	54	
	175	+4	1.1	175	+1	0.233	175	162	
			2.2	175	+2	0.088	114	110	
			3.3	175	+3	0.017	90	94	
			4.4	175	+4	0.002	74	76	
			5.4	175	+5	0.000	68	64	
204	+5	0.9	204	+1	0.226	204	188		
		1.7	204	+2	0.098	134	138		
		2.6	204	+3	0.024	103	110		
		3.4	204	+4	0.003	88	94		
		4.3	204	+5	0.000	74	76		

3.2. TDMA measurements and data reduction procedure

Fig. 5b provides an example of a TDMA spectra measured at a fixed DMA-1 voltage of $V = 0.478$ kV, which corresponds to an electrical mobility of 4.5×10^{-11} C cm/dyn s. The corresponding charged particles as shown in Table 1 are expected to be classified as 75 nm ($p = +1$), 113 nm (+2), 145 nm (+3), 175 nm (+4), and 204 nm (+5), and are computed from the dependence of electrical mobility on particle size.

However, once particles exiting DMA-1 (all with equivalent electrical mobility) are exposed to the Po-210 neutralizer, the resulting redistribution of charge, means that the particles no longer have equivalent electrical mobilities and are therefore resolved when passed through DMA-2. This is symbolically represented at the bottom of Fig. 4. The measured peaks determined by DMA-2 actually appeared at 76, 110, 138, 162, and 188 nm, respectively, and are in very good agreement with the above prediction based on calculation by Eq. (1). The agreement between theory and experiment is degraded with increasing particle size because the theory assumes that particles are spherical, while the larger particles are generally agglomerated.

In the spectra we also observe three smaller peaks in the range of 50–70 and 84–100 nm. These arise from multiply charged particles, which acquired their multiple charge when exposed to the Po-210. These additional smaller peaks

are easily accounted for as seen in Table 1. The two smaller peaks in the range of 50–70 nm are calculated to have 76 nm (+2), 113 nm (+3), and 145 nm (+4) and the third peak in the range of 84–100 nm have 145 nm (+2), 175 nm (+3), and 204 nm (+4) particles. In a later section of this paper we reproduce the spectrum theoretically.

To obtain the number concentration of singly charged particles associated with each peak on the DMA-2 spectra, the contribution from multiply charged larger particles must be removed. For example, the fraction of singly charged particles (f_1) with an equivalent mobility particle diameter of 75 nm was determined by taking the number concentration in the first peak ($N_I(75, 110, 138, 162, 188$ nm)) in Fig. 5b and subtracting all highly charged particles with larger particles as shown below (see Table 1):

$$\begin{aligned}
 N_I(75 \text{ nm}) &= N_I(75, 110, 138, 162, 188 \text{ nm}) \\
 &- \left[\left\{ N_{II}(110, 162, 188 \text{ nm}) - N_{IV}(162 \text{ nm}) f_{2,B} \right. \right. \\
 &\quad \left. \left. - N_V(188 \text{ nm}) f_{3,B} \right\} f_{2,B} \right] \\
 &- \left[\left\{ N_{III}(138, 188 \text{ nm}) - N_V(188 \text{ nm}) f_{2,B} \right\} f_{3,B} \right] \\
 &- \left[N_{IV}(162 \text{ nm}) f_{4,B} \right] - \left[N_V(188 \text{ nm}) f_{5,B} \right], \quad (4)
 \end{aligned}$$

where subscripts I, II, III, IV, and V are the sequence of peaks shown in Fig. 5b.

The fractions ($f_{p,B}$) of multiply charged particles with different sizes are calculated based on Eq. (2) under the assumption of Boltzmann equilibrium for particles exposed

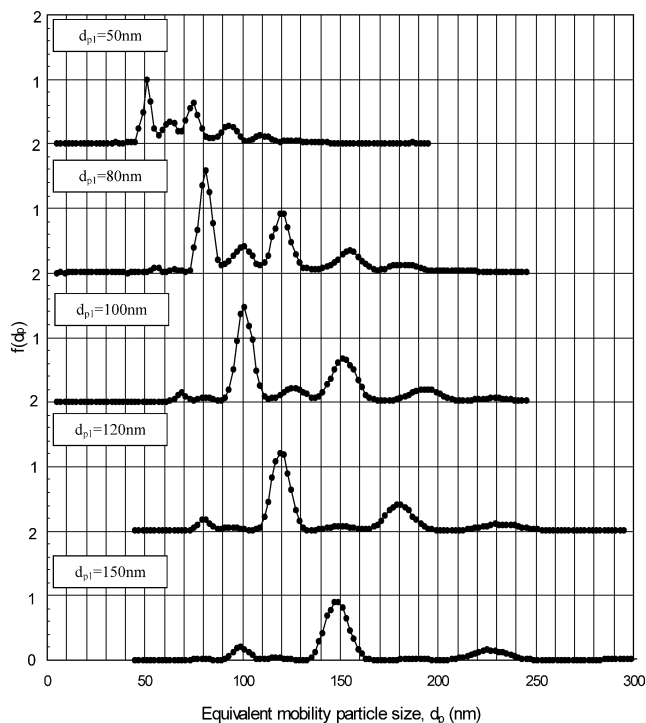


Fig. 6. Example spectra of negatively charged particle size distributions measured by DMA-2 for different DMA-1 voltages (corresponding mobility diameters from DMA-1 are labeled as d_{p1}).

to Po-210. The total number concentration of particles of 75 nm, $N_T(75 \text{ nm})$, was previously measured with the DMPS system. Thus, the fraction (f_1) of singly charged particles with 75 nm diameter can be determined by taking the ratio of $N_1(75 \text{ nm})$ to $N_T(75 \text{ nm})$. To determine the doubly charged fraction (f_2) of 75 nm particles, the DMA-1 voltage was changed to select an electrical mobility corresponding to a doubly charged 75 nm diameter particle.

To obtain the overall particle charge distribution, these procedures were repeated for varying DMA-1 voltages corresponding to the equivalent mobility sizes of 50 to 200 nm. By switching the DMA polarity, the fraction of negatively charged particles could be obtained in the same manner. From these series of TDMA measurements, the relationship between particle size and charge fractions could be decoupled. Fig. 6 presents various spectra of negatively charged particle size distribution at different DMA-1 voltages. We can see from these spectra that more peaks appear for those spectra taken at smaller mobility diameters (d_{p1}). This is due to the fact that at the larger mobility diameters the number concentration was too low to observe multiply charged ($p \geq 3$) spectra. Thus, the fraction of triply or more highly charged particles were not able to be determined over the full size range characterized (50–200 nm). To verify the experimental approach and data reduction procedure, we performed the same experiments on the charge and size distribution of NaCl particles at room temperature. Unlike the soot experiments, salt particles were first passed through ionizing radioactive source (Po-210) to obtain a known Boltzmann

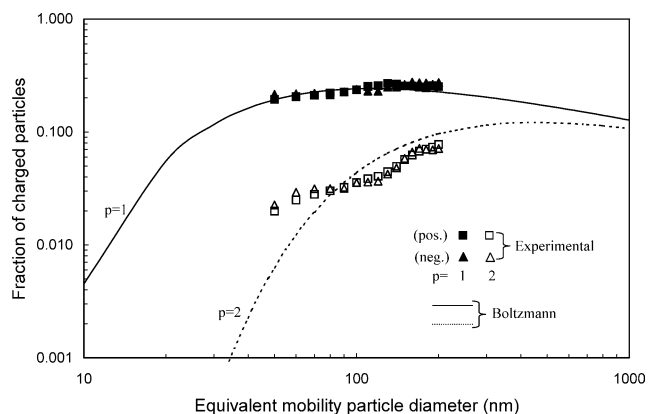


Fig. 7. Charge distribution of Boltzmannized NaCl particles as a function of particle size.

equilibrium charge distribution. Fig. 7 shows the measured charge fraction of NaCl particles of both polarities as a function of particle size as measured by the TDMA system. The measured charge distribution of NaCl particles are in very good agreement with the Boltzmann charge distribution, and indicate that the TDMA technique and data reduction procedure are valid.

3.3. Comparison of TDMA measurements with theory

By applying the TDMA system to the diffusion flame, the charge distribution of soot particles was determined as shown in Fig. 8. To determine the fraction of uncharged particles (f_0), an electrostatic precipitator (ESP) was used to remove all the charged particles prior to DMA-1. The ESP is composed of an expander inlet, a cylindrical electrode, and converging nozzle outlet, in a cylindrical stainless steel housing. It is designed to remove both positively and negatively charged particles by applying a high voltage (10 kV) to the central electrode and grounding the flow tube. In the DMPS mode, the size distribution of flame soot particles was measured with (N_0) and without (N_T) the ESP.

As shown in Fig. 8a, the fraction (f_0) of uncharged particles was obtained by taking the ratio of N_0 to N_T as a function of equivalent mobility diameter. The fraction of uncharged particles (f_0) is shown to be inversely proportional with particle size and varies from about 40% uncharged at 50 nm to about 10% at 200 nm. This result is expected and comes about simply due to the higher surface area available for ion and electron collection for the larger diameter particles. Fig. 8b shows that the fraction of singly and doubly charged particles measured by the TDMA are in good agreement with Boltzmann equilibrium charge distribution evaluated at the flame tip temperature. However, the discrepancy between experimental and theoretical results gets worse with increasing particles size. One can speculate that if the charging process in a flame is limited by kinetic rates than an assumption implicit in the application of Boltzmann theory, namely that the ion attachment (or detachment) coefficients for bipolar ions with charged particles of either same

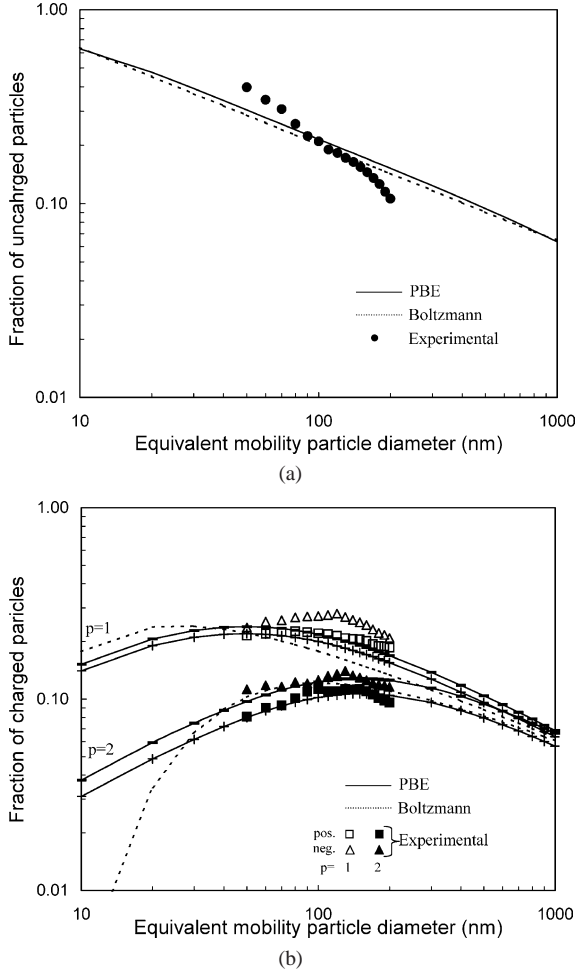


Fig. 8. Charge distribution of flame soot particles as a function of particles size; comparison with PBE and Boltzmann analysis (PBE calculation conditions: $n^+ = n^- = 3.50 \times 10^{11} \text{ cm}^{-3}$, $n_e = 1.5 \times 10^7 \text{ cm}^{-3}$, $T = 1300 \text{ K}$, $Z_i^+ = 2.00 \text{ cm}^2 \text{ V}^{-1} \text{ s}^{-1}$, $Z_i^- = 2.12 \text{ cm}^2 \text{ V}^{-1} \text{ s}^{-1}$, $Z_e = 4000 \text{ cm}^2 \text{ V}^{-1} \text{ s}^{-1}$).

or opposite sign are the same, may yield significant errors when the properties of bipolar ions are unequal [28].

The ions generated by chemi-ionization in the lower part of the flame are believed to cause incipient soot particles to achieve an equilibrium charge corresponding to the local flame temperature [23]. In the upper part of the flame however, the evolution of particle charge is expected to occur from ions and electrons due to ion/electron impact on particles and coagulation of oppositely charged particles. The neutralization process of particles can be thought of a result of both ion/electron impact and bipolar coagulation mechanisms.

We can estimate the expected relative role of the various charging mechanism through an analysis of the characteristic times for the individual processes. The characteristic time for particle charging by ion/electron impact [29] can be estimated by

$$\tau_p = n_i^{-1} c_i^{-1} S^{-1} \cong 10^{-7} - 10^{-6} \text{ s}, \quad (5)$$

where n_i is the number concentration of ions measured by the Langmuir probe ($\sim 10^{11} \text{ cm}^{-3}$), c_i is the thermal velocity of ions, and S is particle surface area.

The characteristic time for ion–ion interactions is calculated by

$$\tau_i = \gamma^{-1} n_i^{-1} \cong 10^{-6} - 10^{-5} \text{ s}, \quad (6)$$

where γ is the ion attachment coefficient in flames ($\sim 10^{-7} \text{ cm}^3 \text{ s}^{-1}$) [19].

The characteristic time of bipolar coagulation [30] was estimated as

$$\tau_c = k_{ij}^{-1} n_p^{-1} \cong 10^{-4} - 10^{-2} \text{ s}, \quad (7)$$

where

$$k_{ij} = \frac{8\pi\epsilon_0}{3\mu} (p_r E)^2 (r_i r_j) (r_i + r_j),$$

n_p is the total number concentration of particles, ϵ_0 the permittivity of free space, μ the gas viscosity, E the electric field strength of the particle ($= pe/r^2$), $p_r = 3\epsilon_r/(\epsilon_r + 2)$, ϵ_r the relative dielectric constant of carbon, and r_i and r_j are the particle radii, where particles are assumed to be monodisperse ($r = r_i = r_j$).

From the comparison of characteristic times, we note that the time for bipolar coagulation is much slower, indicating that the effects of coagulation on particle charge in flames can be neglected. We note that the rapid dilution in the sampling probe was also designed to reduce coagulation effects.

Thermionic emission is also known to be an important mechanism for particle charging in hydrocarbon flames. However, the number concentration of electrons measured by the Langmuir probe were found to be several orders of magnitude smaller than that of bipolar ions. This presumably, results from the fact that in the region of our sampling, the flame temperature is relatively low so that thermionic emission on particle charge can be neglected.

On the basis of our conclusion that ion/electron impact is the dominant particle charging mechanism, we develop a set of population balance equations (PBE), which are based on the work of Marlow and Brock [31] and modified to account for particle–electron interactions. The later interaction is modeled with ion attachment coefficients based on Fuchs [28] theory.

$$\frac{dN_p^\pm}{dt} = K_{1,p+1} n^\mp N_{p+1}^\pm - K_{1,p} n^\mp N_p^\pm + K_{2,p-1} n^\pm N_{p-1}^\pm - K_{2,p} n^\pm N_p^\pm + K_{e,p-1} n_e N_{p-1}^\pm - K_{e,p} n_e N_p^\pm, \quad (8)$$

where $K_0 = 4\pi D_i^\pm a F$, $K_e = 4\pi D_e a F$,

$$K_{2,p}^\pm = \frac{K_0}{\left[\frac{4D_i^\pm a}{c_i^\pm (\delta^\pm)^2} \exp\left(\frac{e\phi_p(\delta)}{kT}\right) + \frac{akT}{pe^2} \left(\exp\left(\frac{pe^2}{kT\delta^\pm}\right) - 1\right) \right]},$$

$$K_{1,p}^\pm = \frac{K_0}{\left[\frac{4D_i^\pm a}{c_i^\pm (\delta^\pm)^2} \exp\left(\frac{-e\phi_p(\delta)}{kT}\right) - \frac{akT}{pe^2} \left(\exp\left(\frac{-pe^2}{kT\delta^\pm}\right) - 1\right) \right]},$$

$$K_{e,p}^- = \frac{K_e}{\left[\frac{4D_e a}{c_e (\delta_e)^2} \exp\left(\frac{e\phi_p(\delta)}{kT}\right) + \frac{akT}{pe^2} \left(\exp\left(\frac{pe^2}{kT\delta_e}\right) - 1\right) \right]},$$

$$K_{e,p}^+ = \frac{K_e}{\left[\frac{4D_e a}{c_e (\delta_e)^2} \exp\left(\frac{-e\phi_p(\delta)}{kT}\right) - \frac{akT}{pe^2} \left(\exp\left(\frac{-pe^2}{kT\delta_e}\right) - 1\right) \right]},$$

where

$$\phi_p(\delta) = \frac{pe}{\delta} - \frac{ea^3}{2\delta^2(\delta^2 - a^2)},$$

$$\delta^\pm = \frac{a^3}{(\lambda_i^\pm)^2} \left[\frac{1}{5} \left(1 + \frac{\lambda_i^\pm}{a}\right) - \frac{1}{3} \left(1 + \left(\frac{\lambda_i^\pm}{a}\right)^2\right) \left(1 + \frac{\lambda_i^\pm}{a}\right)^3 + \frac{2}{15} \left(1 + \left(\frac{\lambda_i^\pm}{a}\right)^2\right)^{5/2} \right],$$

F is interpolation factor for the entire particle size regime [32] ($= \frac{1+\text{Kn}}{1+1.71\text{Kn}+1.33\text{Kn}^2}$), a the particle radius, D_i^\pm the diffusion coefficient of ions, D_e the diffusion coefficient of electron, \bar{c}_i^\pm the thermal velocity of ions, c_e thermal velocity of electron, Kn is Knudsen number ($= 2\lambda/d_p$), N_p^\pm the number concentration of positive and negative aerosol particles of equal size, n^\pm the number concentration of positive and negative ions, n_e the number concentration of electrons, $K_{2,p}$ the attachment coefficient of ions on particles having p charges of the same sign, $K_{1,p}$ the attachment coefficient of ions on particles having p charges of the opposite sign, $K_{e,p}$ the attachment coefficient of electrons on particles having p charges, λ_i^\pm the mean free path of ions and λ_e the mean free path of electron.

The L.H.S. term in Eq. (8) represents the rate of change of number concentration of particles carrying p charges. The particles carrying $p+1$ charge interacting with oppositely charged ions (first term in R.H.S.) and particles carrying $p-1$ charge interacting with same sign of ions (third term in R.H.S.) are the production terms of the particles carrying p charges. At the same time, p charged particles interacting with both polarities of ions are dissipation terms (second and forth term in R.H.S.) for particles carrying p charges. Two additional production and dissipation terms were added to account for the interaction between particles and electrons (fifth and sixth terms in R.H.S.). The charge distribution equation was then derived under the assumption of steady-state condition by taking dN_p/dt (L.H.S. term in Eq. (8)) as zero ($dN_p/dt = 0$). Also the number concentration of particles with higher than $|p|+1$ charges was assumed to be zero, namely $N_{p+1}^\pm = N_{p+2}^\pm = \dots = 0$ [33].

$$f_p^\pm = \frac{N_p^\pm}{N_T} = \frac{\prod_{i=1}^p A_i^\pm}{1 + \sum_{p=1}^\infty (\prod_{i=1}^p A_i^+ + \prod_{i=1}^p A_i^-)}, \quad (9)$$

where $\prod_{i=1}^p A_i^\pm = N_p^\pm / N_0^\pm$,

$$A_p^\pm = \frac{N_p^\pm}{N_{p-1}^\pm} = \left(\frac{n^\pm}{n^\mp}\right)$$

$$\times \frac{K_{2,p-1}^\pm + K_{e,p-1}^\pm \left(\frac{n_e}{n^\pm}\right)}{K_{1,p}^\mp + \left(\frac{n^\pm}{n^\mp}\right) K_{2,p}^\pm + K_{e,p}^\mp \left(\frac{n_e}{n^\mp}\right) - (N_{p+1}^\pm / N_p^\pm) K_{1,p-1}^\mp}.$$

When the number concentration of electrons is zero, Eq. (9) is exactly the same as the general solution suggested by Hussin et al. [33]. As seen in Eq. (9), the fraction of charged particles at steady state is strongly dependent on the relative number of ions and electrons and the ion attachment coefficient. Here, the temperature and ion/electron concentration measurements were applied to calculate the ion attachment coefficient and the charge fraction of particles.

To determine the ion properties including diffusion coefficient, thermal velocity, and mean free path of chemi-ions in flames, it is necessary to know the electrical mobilities. Kinbara et al. [34] measured a value of about $1 \text{ cm}^2 \text{ V}^{-1} \text{ s}^{-1}$ for the electrical mobility of positive ion in flames at 1000 K, while Bradely and Ibrahim [35] obtained a value of $8.2 \text{ cm}^2 \text{ V}^{-1} \text{ s}^{-1}$ at 1730 K, under the assumption of the positive ion carrier being H_3O^+ . In the basis of H_3O^+ as the primary cation, the mobility of the negative ions, OH^- , was obtained ($Z_i \propto M_i^{-1/2}$), as suggested by Kennard [36]. For the electrical mobility of electron in flames we use a value of $4000 \text{ cm}^2 \text{ V}^{-1} \text{ s}^{-1}$ [37].

Ion diffusion coefficient are then obtained from the Einstein relation:

$$D_i = kT Z_i / e. \quad (10)$$

The mean free path of chemi-ion was determined from Maxwell–Chapmann–Enskog theory [38],

$$\lambda_i = \frac{D_i}{(1 + \varepsilon) \frac{3\pi}{8\sqrt{8}} \left(\frac{m_i + m_j}{m_j}\right)^{1/2} \bar{c}_i}, \quad (11)$$

where m_i is the mass of ion, m_j is the mass of air molecule, D_i is the diffusion coefficient of chemi-ion in air, ε is the correction factor when the colliding molecule is assumed to be hard spheres of unequal mass ($= 0.132$), and \bar{c}_i is the thermal velocity of the ion ($= (8kT/\pi m_i)^{1/2}$).

The fraction of uncharged and charged particles calculated by the PBE with various electrical mobilities of chemi-ion was compared with the TDMA data of the particle charge distribution, to determine the optimum chemi-ion properties. Poor agreement was observed when values for electrical mobility suggested by Bradely and Ibrahim [35] were used, but the results got considerably better with the values suggested by Kinbara et al. [34]. The optimum chemi-ion properties to obtain the best agreement are given in Table 2. With the ion properties determined, the fraction of uncharged and charged particles calculated by the PBE along with the TDMA results show good agreement and are presented in Fig. 8b.

For the fraction of singly and doubly charged particles, the results are in best agreement for particles smaller than 100 nm. We suspect that larger particles which are fractal-like aggregates of small primary particles (20–30 nm primaries) may have a lower neutralization rate due to the screening of some parts of the structure. Also, the high concentration of flame soot particles presumably is a sink for

Table 2
Chemi-ion properties in flames

		Kinbara et al. [34]	Bradely and Ibrahim [35]	This work
Flame temperature (K)	T	1000	1730	1300
Electrical mobility ($\text{cm}^2 \text{V}^{-1} \text{s}^{-1}$)	Z_i^+ Z_i^-	1.00 1.06 ^a	8.20 8.67 ^a	2.00 2.12 ^a
Molecular weight (amu)	M_i^+ M_i^-	19* 17*	19 17	19 17
Diffusion coefficient ($\text{cm}^2 \text{s}^{-1}$)	D_i^+ D_i^-	0.086 0.091	1.22 1.30	0.22 0.24
Mean free path (cm)	λ_i^+ λ_i^-	1.34×10^{-6} 1.37×10^{-6}	1.44×10^{-5} 1.47×10^{-5}	3.05×10^{-6} 3.12×10^{-6}
Mean thermal velocity (cm s^{-1})	\bar{c}_i^+ \bar{c}_i^-	1.05×10^5 1.11×10^5	1.39×10^5 1.47×10^5	1.20×10^5 1.27×10^5

^a Calculated values based on $Z_i \propto M_i^{-1/2}$ [36] under the assumption of H_3O^+ (ion mass $M_i^+ = 19^*$) for positive ion carrier and OH^- (ion mass, $M_i^- = 17^*$) for negative ion carrier.

ions and electrons so that the neutralization rate would be retarded, and hence the charge state of particles would remain slightly higher than equilibrium for the corresponding flame temperature. Furthermore, the simple PBE equation could not account for nonideal interactions between ions (or electrons) and particles and the complexity of flame ionization processes.

Using our assumption of chemi-ions with unequal properties, we reproduced the size distributions of soot particles to verify whether the data reduction procedure and chemi-ion properties used are reasonable. To do so, the peak positions were first calculated using the electrical mobility expression (Eq. (1)). Then the number concentration of particles at each peak was computed based on the multiple charging correction (see Eq. (4) example). Finally, we fit the spectra by assuming that the particle size distribution after the TDMA system can be reasonably approximated with a Gaussian [10],

$$G(d_p) = \frac{N}{\sigma\sqrt{2\pi}} \exp\left(-\frac{1}{2}\left(\frac{d_p - \bar{d}_m}{\sigma}\right)^2\right). \quad (12)$$

The full-width half-maximum (FWHM) of the Gaussian function is given by [39]

$$\text{FWHM} = 2\sigma\sqrt{2\ln 2}. \quad (13)$$

For simplicity, we also assume a perfect triangular transfer function for the DMAs. Thus, the FWHM of the DMA transfer function is given by [40]

$$\text{FWHM} = \frac{Q_a}{Q_c} \bar{d}_m, \quad (14)$$

where Q_a is the aerosol flow rate, Q_c is the sheath flow rate, and \bar{d}_m is the mean diameter.

To obtain the standard deviation of the Gaussian fitting function, we combined Eq. (13) with Eq. (14), which yields

$$\sigma = \frac{Q_a}{Q_c} \frac{\bar{d}_m}{2(2\ln 2)^{1/2}}. \quad (15)$$

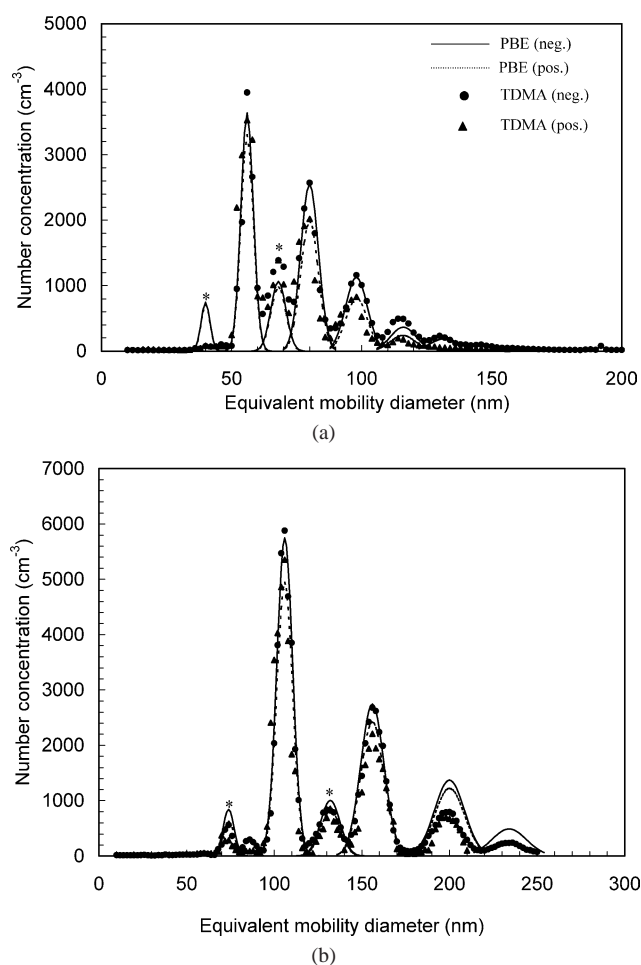


Fig. 9. Comparison the particle size distribution measured by TDMA with that calculated by population balance equation at (a) $d_{p1} = 50$ nm and (b) $d_{p1} = 100$ nm.

As can be seen in Fig. 9, for the two different mobility sizes in DMA-1, the particle size distributions (PSD) reproduced by the PBE with unequal ion properties for chemi-ions, are in reasonably agreement with the PSD measured by the

TDMA. In general we observe a higher number concentration of negatively charged particles, which the model shows results from the higher electrical mobility of negative ion. Electrons, which would also be expected to enhance the formation rate of negatively charged particles, are unimportant in this regime due to the relatively low electron concentration compared with negative ions. The spectral reproduction was also able to identify additional peaks (* marked in Fig. 9), which do not arise from the flame charging process, but rather is associated with large multiply charged particles, created in the Po-210 neutralizer.

4. Summary and conclusion

A modified tandem differential mobility analysis (TDMA) technique is developed to measure the charge fraction of nanosized aerosols. Nanoaerosol particles extracted from an atomizer and a combustion flame are selected with the first DMA to give particles of a single electrical mobility. These particles are then subjected to a bipolar gas-phase ion bath to redistribute the charge to a Boltzmann distribution. These particles are then sent to a second mobility analyzer to give a particle size and charge spectra corresponding to the initially selected mobility diameter. This procedure is repeated for different mobility sizes. A data analysis procedure is presented to invert the data to give the charge distribution as a function of equivalent mobility particle diameter ranging from 50 to 200 nm. The validation of the TDMA method for determining charge distribution was experimentally verified with Boltzmann equilibrium theory for nanosized NaCl and soot particles produced by a Collison atomizer and a diffusion flame, respectively.

Better agreement was found for highly charged flame generated nanosized carbonaceous soot aerosol particles using a population balance equation (PBE) approach combined with Fuchs theory where ion–particle and electron–particle combination was precisely accounted for. Various chemi-ion properties in hydrocarbon flames were tested to find optimum values by comparing the charge fraction curves calculated with those measured by the TDMA. The optimum chemi-ion properties were additionally found to be in good agreement with the values suggested by Kinbara et al. [34].

The TDMA technique described can be extended to measure the charge and size distributions of various nanoaerosol sources as well as practical combustion systems.

Appendix A. Nomenclature

a	particle radius
\bar{c}_i^\pm	thermal velocity of ions
\bar{c}_e	thermal velocity of electron
C_c	Cunningham slip correction factor
D_i^\pm	diffusion coefficient of positive and negative ions
D_e	diffusion coefficient of electron

d_p	equivalent mobility particle diameter
d_{p1}	equivalent mobility size of singly charged particle determined at DMA-1 voltage
E	electric field strength of particle
e	elementary electrical charge ($= 1.6 \times 10^{-19}$ C)
$f_{p,B}$	charge fraction of Boltzmannized particle carrying p charge
f_p	charge fraction of particle carrying p charge
i_d	electrical current induced from flame ions
Kn	Knudsen number ($= 2\lambda/d_p$)
k	Boltzmann constant ($= 1.38 \times 10^{-23}$ J/K)
$K_{2,p}$	attachment coefficient of ions on particles having p charges of the same sign
$K_{1,p}$	attachment coefficient of ions on particles having p charges of the opposite sign
$K_{e,p}$	attachment coefficient of electron on particles having p charges
k_{ij}	bipolar coagulation rate
N_p^\pm	number concentration of positive and negative aerosol particles of equal size
N_T	total number concentration at a given mobility size
n^\pm	number concentration of positive and negative ions
n_e	number concentration of electron
n_p	total number concentration of particles
p	number of elementary units of charge
r	particle radius
r_p	radius of Langmuir probe
S	particle surface area
T	absolute temperature
t	time
V	applied electric potential on DMA electrode
Z_e	electrical mobility of electron
Z_i	electrical mobility of ion
ϕ	work function of material
γ	ion recombination constant
λ	mean free path of air
λ_e	mean free path of electron
λ_i^\pm	mean free path of ions
μ	air viscosity

References

- [1] F.K. Hurd, J.C. Mullins, J. Colloid Sci. 17 (1962) 91.
- [2] M. Adachi, B.Y.H. Liu, D.Y.H. Pui, Part. Part. Syst. Charact. 8 (1990) 200.
- [3] D. Wake, A. Thorpe, G.J. Bostock, J.K.W. Davies, R.C. Brown, J. Aerosol Sci. 22 (1991) 901.
- [4] B. Forsyth, B.Y.H. Liu, F.J. Romay, Aerosol Sci. Tech. 128 (1998) 489.
- [5] J. Porstendörfer, A. Hussin, H.G. Scheibel, K.H. Becker, J. Aerosol Sci. 15 (1) (1984) 47.
- [6] K.C. Moon, Charging mechanism of submicron diesel particles, Ph.D. thesis, University of Minnesota, 1984.
- [7] R.J. Santoro, J.H. Miller, Langmuir 3 (1987) 244.
- [8] K.H. Ahn, S.H. Sohn, C.H. Jung, M. Choi, Scripta Mater. 44 (2001) 1889.
- [9] B.Y.H. Liu, D.Y.H. Pui, K.T. Whitby, D.B. Kittelson, Y. Kousaka, R.L. McKenzie, Atmos. Environ. 12 (1–3) (1978) 99.

- [10] D.J. Rader, P.H. McMurry, *J. Aerosol Sci.* 17 (5) (1986) 771.
- [11] K.J. Higgins, H. Jung, D.B. Kittelson, J.R. Roberts, M.R. Zachariah, *J. Phys. Chem.* 106 (2002) 96.
- [12] R.J. Santoro, H.G. Semerijan, R.A. Dobbins, *Combust. Flame* 51 (1983) 203.
- [13] M. Kasper, K. Siegmann, K. Sattler, *J. Aerosol Sci.* 28 (8) (1997) 1569.
- [14] G.S. Hewitt, *Trans. Am. Inst. Elect. Eng.* 76 (1957) 300.
- [15] B.Y.H. Liu, D.Y.H. Pui, *J. Colloid Interface Sci.* 49 (1974) 305.
- [16] E.O. Knutson, K.T. Whitby, *J. Aerosol Sci.* 6 (6) (1976) 443.
- [17] W.C. Hinds, *Aerosol Technology: Properties, Behaviors, and Measurement of Airborne Particles*, Wiley, 1982.
- [18] M.R. Stolzenberg, P.H. McMurry, *TDMAFIT User's Manual*, PTL publication No. 653, University of Minnesota, 1988.
- [19] B.E. Travers, H. Williams, *Proc. Combust. Inst.* 10 (1965) 657.
- [20] H.F. Calcote, *Proc. Combust. Inst.* 12 (1969) 184.
- [21] L.B. Loeb, *Basic Processes of Gaseous Electronics*, Univ. of California Press, Berkeley/Los Angeles, 1961.
- [22] J. Deckers, A. Van Tiggelen, *Proc. Combust. Inst.* 7 (1959) 254.
- [23] P.F. Knewstubb, T.M. Sugden, *Proc. Combust. Inst.* 7 (1959) 247.
- [24] Ph. Gerhardt, K.U. Homman, *Ber. Bunsenges. Phys. Chem.* 94 (1990) 1086.
- [25] J. Dawe, S.A.H. Rizvi, P.R. Smy, *IEEE Trans. Plasma Sci.* 21 (1993) 202.
- [26] J. Guo, J.M. Goodings, *Chem. Phys. Lett.* 329 (2000) 393.
- [27] H. Fissan, C. Helsper, H.J. Thielen, *J. Aerosol Sci.* 14 (1983) 354.
- [28] N.A. Fuchs, *Geofis. Pura Appl.* 56 (1963) 185.
- [29] V.A. Schweigert, I.V. Schweigert, *J. Phys. Appl. Phys.* 29 (1996) 655.
- [30] B. Eliasson, W. Egli, *J. Aerosol Sci.* 22 (4) (1991) 429.
- [31] W.H. Marlow, J.R. Brock, *J. Colloid Interface Sci.* 51 (1975) 23.
- [32] N.A. Fuchs, A.G. Sutugin, *Highly Dispersed Aerosol*, Ann Arbor Science, 1971.
- [33] A. Hussin, H.G. Scheibel, K.H. Becker, J. Porstendörfer, *J. Aerosol Sci.* 14 (5) (1983) 671.
- [34] T. Kinbara, J. Nakamura, H. Ikegami, *Proc. Combust. Inst.* 7 (1959) 263.
- [35] D. Bradely, S.M.A. Ibrahim, *J. Phys. D Appl. Phys.* 7 (1974) 1377.
- [36] E.H. Kennard, *Kinetic Theory of Gases*, McGraw–Hill, New York, 1938, p. 483.
- [37] L.S. Frost, *J. Appl. Phys.* 32 (1961) 2029.
- [38] J. Bricard, *Problems of Atmospheric and Space Electricity*, Elsevier, Amsterdam, 1965, p. 82.
- [39] W.R. Leo, *Techniques for Nuclear and Particle Physics Experiments*, Springer-Verlag, 1992.
- [40] E.O. Knutson, K.T. Whitby, *J. Aerosol Sci.* 6 (1975) 443.